Journal of Zhejiang University-SCIENCE A (Applied Physics & Engineering)
ISSN 1673-565X (Print); ISSN 1862-1775 (Online)
www.jzus.zju.edu.cn; www.springerlink.com
E-mail: jzus@zju.edu.cn

# Engineered metabarrier as shield from longitudinal waves: band gap properties and optimization mechanisms*

Xi SHENG[1,2], Cai-you ZHAO[1,2], Qiang YI[1,2], Ping WANG[†‡1,2], Meng-ting XING[1,2]

[1]*MOE Key Laboratory of High-speed Railway Engineering, Southwest Jiaotong University, Chengdu 610031, China*

[2]*School of Civil Engineering, Southwest Jiaotong University, Chengdu 610031, China*

[†]E-mail: wping@swjtu.edu.cn

Received Apr. 12, 2017; Revision accepted Dec. 13, 2017; Crosschecked Apr. 13, 2018; Published online May 16, 2018

**Abstract:** Phononic crystals that prevent the propagation of waves in a band gap have been widely applied in wave propagation control. In this paper, we propose the use of a metabarrier, based on a locally resonant phononic crystal mechanism, as a floating-slab track bearing to shield the infrastructure in a floating-slab track system from longitudinal waves from the slab, thereby improving mitigation of ground-borne vibrations. The locally resonant band gap properties of the metabarrier were studied based on the finite element method, and the shielding performance was verified by the transmission spectrum. Simplified models for band gap boundary frequencies were built according to the wave modes. Furthermore, a 3D half-track model was built to investigate the overall vibration mitigation performance of the floating-slab track with the metabarrier. An optimization mechanism for the band gap boundary frequencies is proposed. As the low-frequency ground-borne vibrations induced by subways carry the most energy, multi-objective genetic algorithm optimization was conducted to obtain a lower and wider band gap for a better shielding performance. The results show that the retained vibration isolation performance of the low natural frequency, the shielding performance of the band gap, and the controllability of band gap boundary frequencies all contribute to an improvement in overall vibration mitigation performance. The vertical static stiffness of the metabarrier was close to that of the existing bearing of the floating-slab track. An optimized locally resonant band gap from 50 to 113 Hz was generated using the optimization mechanism.

**Key words:** Metabarrier; Phononic crystal; Band gap; Longitudinal wave; Optimization mechanism
https://doi.org/10.1631/jzus.A1700192 **CLC number:** U213.212

## 1 Introduction

Vertical ground-borne vibrations induced by subways can have an adverse impact on objects such as residential buildings, hospitals, schools, and precision instruments. The frequency range of interest for these vibrations is mainly below 80 Hz (Gupta et al., 2009; Ding et al., 2010). Human comfort can be compromised in residences and office buildings by vibrations below 80 Hz (Sanayei et al., 2013). Therefore, vibration mitigation measures for subways target mainly low-frequency vertical vibrations. As one of a number of common vibration mitigation measures, the floating-slab track (FST) has good vibration isolation performance. The vibration isolation principle (Li and Wu, 2008; Hui and Ng, 2009; Ding et al., 2011) of the FST is to insert a mass-spring system with a low natural frequency between the rail and the infrastructure, which can isolate vibration at frequencies above $\sqrt{2}$ times the natural frequency. The vertical stiffness provided by the bearing should not be too low in consideration of operational safety, but if too high it will weaken the vibration isolation performance. However, the vertical vibration energy

‡ Corresponding author

* Project supported by the National Natural Science Foundation of China (Nos. 51425804 and 51508479) and the Research Fund for the Key Research and Development Projects in Sichuan Province (No. 2017GZ0373), China

ORCID: Xi SHENG, https://orcid.org/0000-0001-5647-8837; Ping WANG, https://orcid.org/0000-0002-8489-5520

transferred from the floating-slab to the infrastructure is carried mostly by the longitudinal waves in the bearing.

Phononic crystals are periodic composite materials that can exhibit elastic wave band gaps (BGs) (Kushwaha et al., 1993; Mead, 1996; Yao et al., 2010; Liu et al., 2015). When elastic waves propagate in phononic crystals, a band structure will form under the effects of the periodicity. The frequency regions between band structure curves form BGs which prohibit elastic wave propagation. Bragg scattering (BS) and local resonance (LR) are two main mechanisms for the creation of BGs (Zhao et al., 2016). The wavelength corresponding to the frequency range of BS BGs has the same order of magnitude as the lattice constant, while the wavelength corresponding to the frequency range of LR BGs is much longer than the lattice constant. Recently, phononic crystal theory was applied in a preliminary track study (Wang et al., 2017) and a periodic control measure of the dynamical track behaviour was studied (Xiao et al., 2017), but those studies focused mainly on the elastic waves which propagate along the longitudinal direction of the track. There have been few phononic crystal applications for shielding from longitudinal waves which travel vertically to the infrastructure in the track. Liu et al. (2016) designed an X-shape structured lever-type isolation system to attenuate low-frequency longitudinal waves, and controlled the BG width and anti-resonance frequency through parameter regulation. Zheng et al. (2011) designed a 1D periodic structure support which realised waveform transformation. Through theoretical derivation and experimental verification, the periodic structure proved to generate overall-frequency-range BGs. Yin et al. (2014) designed a 3D nacreous composite material with a broad low-frequency BG, which can be used to design vibration isolation devices through BG regulation. However, the vertical stiffness of these phononic crystal structures is too low to satisfy the requirement of the FST bearing, and so they cannot be applied to a FST. Moreover, it would be difficult to generate low-frequency BGs within the size limit when the BS BG mechanism is applied. Fortunately, LR phononic crystals (Liu et al., 2003) can obtain low-frequency BGs with a much smaller lattice constant.

In this paper, a metabarrier using a locally resonant phononic crystal mechanism is proposed for use as a FST bearing to improve vibration mitigation performance, shielding infrastructure from low-frequency longitudinal waves which carry large vertical vibration energy and propagate vertically from the floating slab. The metabarrier is designed to supply a vertical static stiffness close to that of existing bearings in the FSTs. Thus, the shielding performance of the BG and the vibration isolation performance of the low natural frequency can simultaneously contribute to the overall vibration mitigation performance of the new FST supported by the metabarrier. The finite element method (FEM) was used in this study to examine the LR BG properties of the metabarrier, and simplified models for BG boundary frequencies were built according to the wave modes. The shielding performance of the LR BG was verified by the transmission spectrum. Furthermore, a 3D half-track model was built to investigate the overall vibration mitigation performance of the FST with the metabarrier. The benefits of the band gap could be studied using the single metabarrier structure and the whole track system. An optimization mechanism for the band gap boundary frequencies was proposed according to the ground-borne vibrations induced by subways. As the low-frequency vibrations carried the most energy, a multi-objective genetic algorithm optimization was used to obtain a lower and wider band gap.

## 2 Proposed metabarrier

The proposed metabarrier is a 1D phononic crystal structure set between the floating slab and the infrastructure (Fig. 1).

Each unit cell of the metabarrier comprises two aluminium alloy connectors, internal rubber, external rubber, and an annular steel resonator (Fig. 2). Two connectors are connected by the internal rubber which has a cup-like shape. The external rubber connects one of connectors to the annular steel resonator.

The external rubber and the annular steel resonator are designed to provide the LR BG while the connectors and internal rubber are designed to provide the vertical stiffness for the floating slab. Fig. 3 shows the geometric size of the unit cell and partial geometric values. Table 1 lists material parameters.

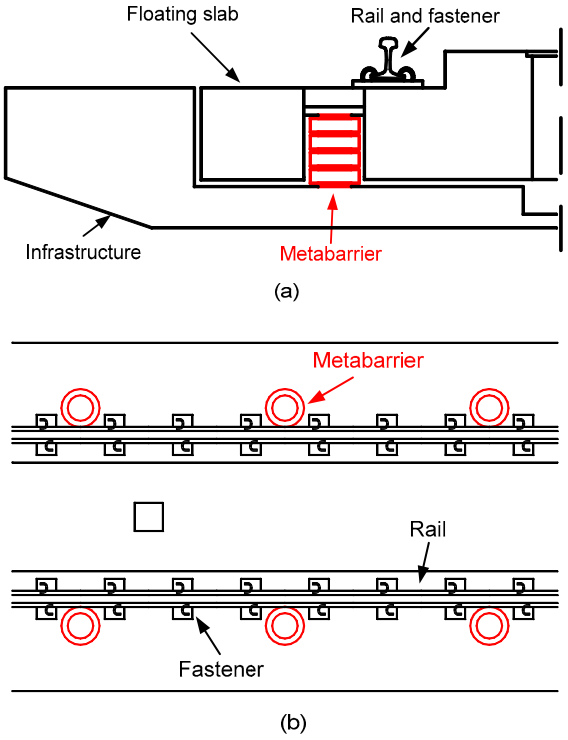


**Fig. 1 Layout of metabarrier in the FST**
(a) Sectional view; (b) Top view

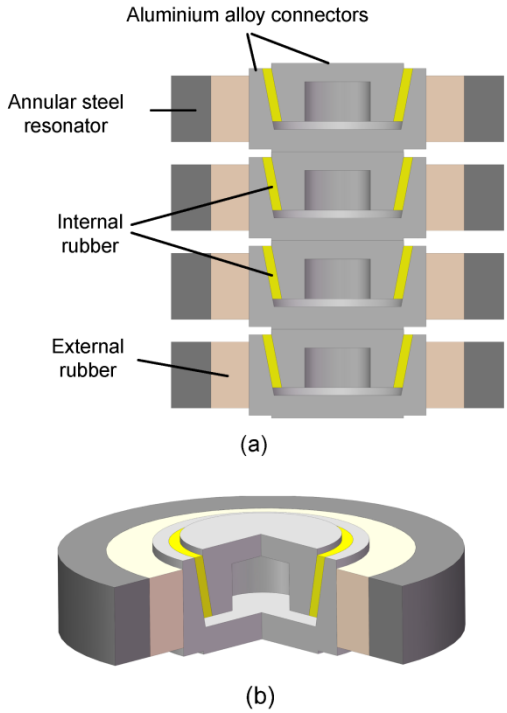


**Fig. 2 Sectional view of the metabarrier (a) and 3/4 cut-away view of a unit cell (b)**

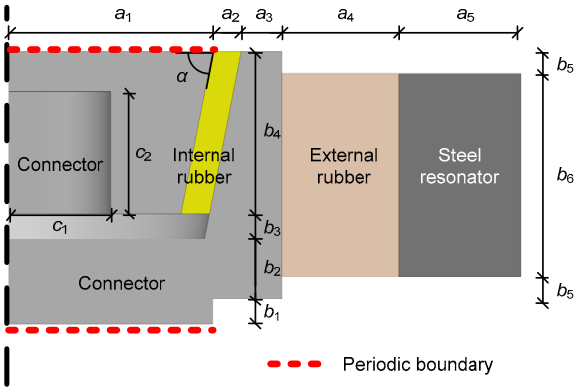


**Fig. 3 Geometry size of the metabarrier unit cell**
Partial geometric parameters can be given as follows: $a_4$=30 mm; $b_1$=6 mm; $b_2$=15 mm; $b_3$=6 mm; $b_4$=40 mm; $b_5$=5.5 mm; $b_6$=50 mm; $c_1$=25 mm; $c_2$=30 mm

**Table 1 Material parameters of the metabarrier unit cell**

| Component | Density (kg/m$^3$) | Elastic modulus (MPa) | Poisson's ratio | Loss factor |
|---|---|---|---|---|
| Connector | $\rho_1$=2700 | $E_1$=70 000 | $\upsilon_1$=0.33 | $\eta_1$=0 |
| Internal rubber | $\rho_2$=1300 | $E_2$=28 | $\upsilon_2$=0.47 | $\eta_2$=1 |
| External rubber | $\rho_3$=1300 | $E_3$=3 | $\upsilon_3$=0.47 | $\eta_3$=0.05 |
| Steel resonator | $\rho_4$=7850 | $E_4$=200 000 | $\upsilon_4$=0.30 | $\eta_4$=0 |

## 3 Band gap properties of the metabarrier

### 3.1 Band structure

When an ideal elastic body (continuous, homogeneous, isotropic, and perfectly elastic) deforms slightly, the governing equation of motion without the body force is expressed as (Eringen and Suhubi, 1975):

$$\rho\frac{\partial^2\boldsymbol{u}(\boldsymbol{r},t)}{\partial t^2}=(\lambda+\mu)\nabla\nabla\bullet\boldsymbol{u}(\boldsymbol{r},t)+\mu\nabla^2\boldsymbol{u}(\boldsymbol{r},t), \quad (1)$$

where $\boldsymbol{u}(\boldsymbol{r}, t)$ is the displacement function vector, $\boldsymbol{r}$ is the coordinate vector, $t$ is the time, $\rho$ is the density, $\lambda$ and $\mu$ are the Lamé constants, $\nabla$ is the Hamilton differential operator, and $\bullet$ is the inner product. The solution of Eq. (1) satisfies the Bloch theorem (Kushwaha et al., 1994):

$$\boldsymbol{u}(\boldsymbol{r},t)=\mathrm{e}^{\mathrm{i}(\boldsymbol{K}\bullet\boldsymbol{r}-\omega t)}\boldsymbol{u}_{\boldsymbol{K}}(\boldsymbol{r}), \quad (2)$$

where $\boldsymbol{K}$ is the wave vector of the reciprocal space, $\boldsymbol{u}_{\boldsymbol{K}}(\boldsymbol{r})$ is the wave amplitude, and $\omega$ is the angular frequency. Considering the periodicity of the structure, $\boldsymbol{u}_{\boldsymbol{K}}(\boldsymbol{r})$ can be expressed as a periodic function (Yan et al., 2015):

$$\boldsymbol{u}_{\boldsymbol{K}}(\boldsymbol{r}+\boldsymbol{R})=\boldsymbol{u}_{\boldsymbol{K}}(\boldsymbol{r}), \tag{3}$$

where $\boldsymbol{R}$ is the periodic constant vector. The periodic boundary conditions can be obtained by substituting Eq. (3) into Eq. (2):

$$\boldsymbol{u}(\boldsymbol{r}+\boldsymbol{R},t)=\mathrm{e}^{\mathrm{i}\boldsymbol{K}\cdot\boldsymbol{R}}\boldsymbol{u}(\boldsymbol{r},t). \tag{4}$$

The eigenvalue problem involving the band structure of an infinite periodic structure can be obtained by applying the periodic boundary conditions (Eq. (4)) to the governing equation (Eq. (1)). To obtain the band structure of the metabarrier, the finite element software COMSOL Multiphysics was adopted to solve the eigenvalue problem. The periodic boundary conditions were set for the surfaces of the unit cell. As the proposed metabarrier is a 1D phononic crystal structure, the irreducible Brillouin zone and the wave vectors which need to be calculated for the band structure are both 1D. Thus, the wave vector was then expressed by the scalar $k$. By selecting the wave vector in the irreducible Brillouin zone (0, $\pi/a$), where $a$ ($=b_1+b_2+b_3+b_4$) is the lattice constant of the unit cell, a series of corresponding $\omega$ can be obtained. The maximum element mesh size was smaller than 0.01 m. The first 10 band structure curves of the metabarrier calculated by the FEM are shown in Fig. 4.

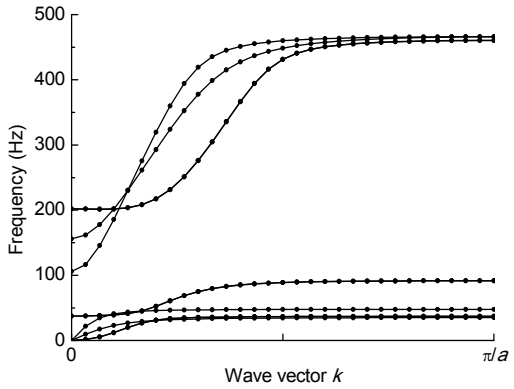


**Fig. 4 The first 10 band structure curves from the metabarrier**

Though all the waves in Fig. 4 propagate along the axial direction (i.e. the vertical direction in the FST system), not all modes correspond to longitudinal waves, which are the major targets of the shielding. The modes of interest must be distinguished from others. When the wave vector $k$ equals $\pi/a$, the displacement vector fields of the first 10 modes of the metabarrier are shown in Fig. 5.

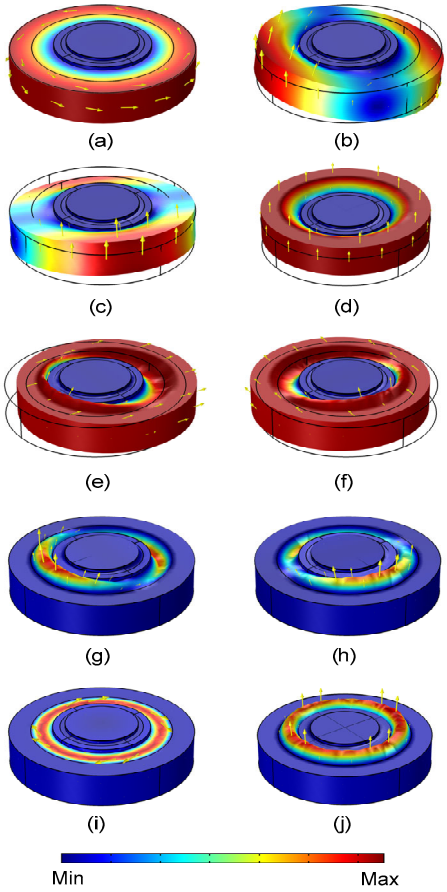


**Fig. 5 Displacement vector fields of the first 10 modes of the metabarrier ($k=\pi/a$)**

(a) 1st (35 Hz): axial rotation of the steel resonator; (b) 2nd (37 Hz): radial rotation of the steel resonator; (c) 3rd (37 Hz): radial rotation of the steel resonator; (d) 4th (48 Hz): axial vibration of the steel resonator; (e) 5th (92 Hz): radial vibration of the steel resonator; (f) 6th (92 Hz): radial vibration of the steel resonator; (g) 7th (460 Hz): radial rotation of the external rubber; (h) 8th (460 Hz): radial rotation of the external rubber; (i) 9th (466 Hz): axial rotation of the external rubber; (j) 10th (466 Hz): axial vibration of the external rubber

The fourth and the tenth modes correspond to the longitudinal waves. The band structure below 500 Hz after mode distinction is shown in Fig. 6.

As a result, the frequency range of the first BG was 48–105 Hz. The mode corresponding to the starting frequency $f_s$ has the wave vector equal to $\pi/a$, while the mode corresponding to the cut-off frequency $f_e$ has the wave vector equal to zero.

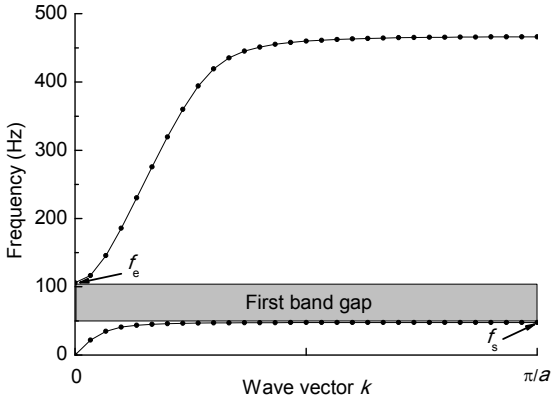


**Fig. 6 Band structure of the metabarrier corresponding to vertical vibrations**

### 3.2 Boundary frequency

To analyse further the boundary frequencies of the first BG, a supercell composed of two unit cells was used. The first BG obtained by the supercell was exactly the same as that obtained by one unit cell. The displacement vector fields of the modes corresponding to the boundary frequencies are shown in Fig. 7.

According to Fig. 7, the starting frequency of the first BG is determined by the resonance of the steel resonator. In this resonance mode, the steel resonators of adjacent unit cells vibrate in inverse directions while the connectors and internal rubber stay still, which realizes the dynamic balance of the whole structure. Thus, the start frequency $f_s$ equals the resonant frequency of the steel resonator. The simplified model of the resonance can be established using a mass-spring system. In this model, the steel resonator is considered as the mass $m_1$, and the shear stiffness $k_1$ of the external rubber is simulated with a linear spring (Fig. 8a).

The cut-off frequency of the first BG is determined by the resonance between the steel resonator and the combination of connectors and internal rubber. In this resonance mode, there is no relative motion between the connectors and the internal rubber. The steel resonator and the combination in the same unit cell vibrate in inverse directions realizing the dynamic balance of the whole structure. Thus, the cut-off frequency $f_e$ equals the antiphase resonance frequency of the steel resonator and the combination. A mass-spring system was adopted to establish a simplified model of this resonant mode. The steel resonator is considered as the mass $m_1$ while the mass sum of the combination is $m_2$. The shear stiffness $k_1$ of the external rubber was also simulated with a linear spring. The simplified model of the cut-off frequency is shown in (Fig. 8b). The result shows that the first BG belongs to a LR BG.

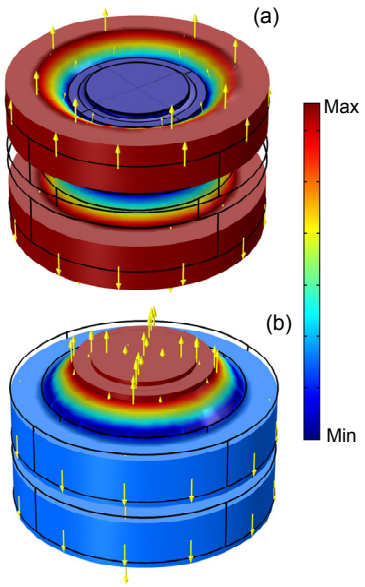


**Fig. 7 Displacement vector fields of the modes corresponding to the starting frequency (a) and the cut-off frequency (b)**

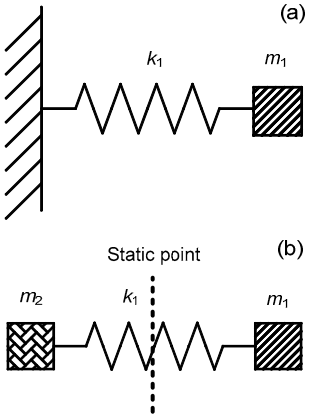


**Fig. 8 Simplified models of the starting frequency (a) and the cut-off frequency (b) in the first BG**

According to material mechanics, the shear stiffness $k_1$ of the external rubber is

$$k_1 = \frac{\pi(a_1 + a_2 + a_3)b_6 E_3}{(1+\upsilon_3)a_4}. \tag{5}$$

The mass $m_1$ of the steel resonator is

$$\begin{aligned} m_1 &= \pi b_6 \rho_4 [(a_1 + a_2 + a_3 + a_4 + a_5)^2 \\ &\quad - (a_1 + a_2 + a_3 + a_4)^2] \\ &= \pi a_5 (2a_1 + 2a_2 + 2a_3 + 2a_4 + a_5) b_6 \rho_4, \end{aligned} \tag{6}$$

and the mass sum of the combination is

$$\begin{cases} m_2 = m_a + m_b, \\ m_a = \rho_1 \pi \{[a_1^2 b_1 + (a_1 + a_2 + a_3)^2 (b_2 + b_3 + b_4)] \\ \quad -\frac{1}{3}\tan\alpha[(a_1 + a_2)^3 - a_1^3 - (a_1 + a_2 - b_4 \cot\alpha)^3 \\ \quad + (a_1 - b_4 \cot\alpha)^3 + (a_1 + a_2 - b_4 \cot\alpha)^3 \\ \quad - (a_1 + a_2 - b_3 \cot\alpha - b_4 \cot\alpha)^3] - c_1^2 c_2\}, \\ m_b = \frac{1}{3}\pi\rho_2 \tan\alpha[(a_1 + a_2)^3 - (a_1 + a_2 - b_4 \cot\alpha)^3 \\ \quad + (a_1 - b_4 \cot\alpha)^3 - a_1^3], \end{cases} \tag{7}$$

where $m_a$ is the mass sum of two connectors and $m_b$ is the mass of the internal rubber. The equation of motion for the simplified model of the starting frequency is

$$m_1 \ddot{u}_1 + k_1 u_1 = 0, \tag{8}$$

where $u_1$ is the displacement of the steel resonator. The equations of motion for the simplified model of the cut-off frequency are as follows:

$$\begin{cases} m_1 \ddot{u}_1 + k_1 (u_1 - u_2) = 0, \\ m_2 \ddot{u}_2 + k_1 (u_2 - u_1) = 0, \end{cases} \tag{9}$$

where $u_2$ is the displacement of the combination. According to the equations of motion, the boundary frequencies of the first gap band are

$$\begin{cases} f_s = \dfrac{1}{2\pi}\sqrt{\dfrac{k_1}{m_1}}, \\ f_e = \dfrac{1}{2\pi}\sqrt{k_1\left(\dfrac{1}{m_1} + \dfrac{1}{m_2}\right)}. \end{cases} \tag{10}$$

The frequency range calculated by Eq. (10) was 47–104 Hz, and the difference between the results of the simplified models and the FEM was only 1 Hz. Thus, the simplified models can be adopted to calculate the boundary frequencies of the first BG. According to Eq. (10), the starting frequency will be affected by parameters which can change the shear stiffness of the external rubber or the mass of the steel resonator, while the cut-off frequency will be affected by parameters which can change the shear stiffness of the external rubber or the mass of the steel resonator, the connectors or the internal rubber. From the simplified models, the elastic modulus of the internal rubber has no effect on the boundary frequencies, but it is essential to the vertical stiffness provided by the metabarrier. Thus, the vertical stiffness and the boundary frequencies can be independent, which is beneficial for the design of a metabarrier in a FST.

### 3.3 Shielding performance of the band gap

The BG properties were studied under the condition of the infinite periodicity. However, the metabarrier comprises only four unit cells. Therefore, a transmission spectrum was used to verify the shielding performance of the BG. To obtain the transmission spectrum of the metabarrier, a harmonic vertical displacement excitation $X_{in}$ was imposed on the upper end of the metabarrier, and on the other end the average displacement response $X_{out}$ was measured (Fig. 9).


**Fig. 9 Transmission spectrum calculation of the metabarrier**

The calculation was conducted using the finite element software COMSOL Multiphysics. The viscous damping model and direct analysis method are employed in the calculation, and the damping is applied in the form of damping loss factors. The transmission spectrum (TS) was defined as

$$\mathrm{TS}=20\lg\left(\frac{|X_{\mathrm{out}}|}{|X_{\mathrm{in}}|}\right). \tag{11}$$

When the longitudinal wave is shielded, the TS is less than zero. In this way, the shielding zones can be obtained. The results of the TSs are shown in Fig. 10.

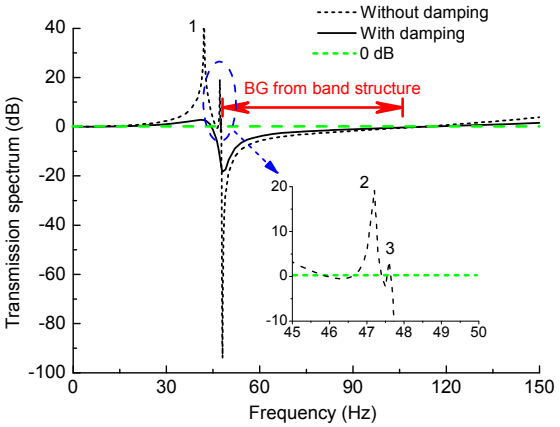


**Fig. 10 Transmission spectra of the metabarrier**

The dashed line and the solid line shown in Fig. 10 refer to the TSs without and with the rubber damping (both internal and external rubber damping) listed in Table 1, respectively. Comparison of Fig. 6 with Fig. 10 shows that the first BG frequency range matched well with the shielding zone obtained by the transmission spectrum. There were three peaks in the calculation condition without damping, and the frequencies of those peaks were 42.1, 47.2, and 47.6 Hz, respectively. Their modes are shown in Fig. 11.

In the mode of peak 1 (42.1 Hz), all the components of the metabarrier vibrate in the same direction though the vibration amplitude of the connectors is much smaller than that of the steel resonators. In the mode of peak 2 (47.2 Hz), the upper two steel resonators vibrate in the same direction, which is opposite to that of the resonator at the bottom. The resonator in the second layer almost stays still. The mode of peak 3 turns out to be the mode corresponding to the starting frequency of the first BG. As damping weakens the resonance of the metabarrier, these peaks cannot be seen in the calculation condition with damping.

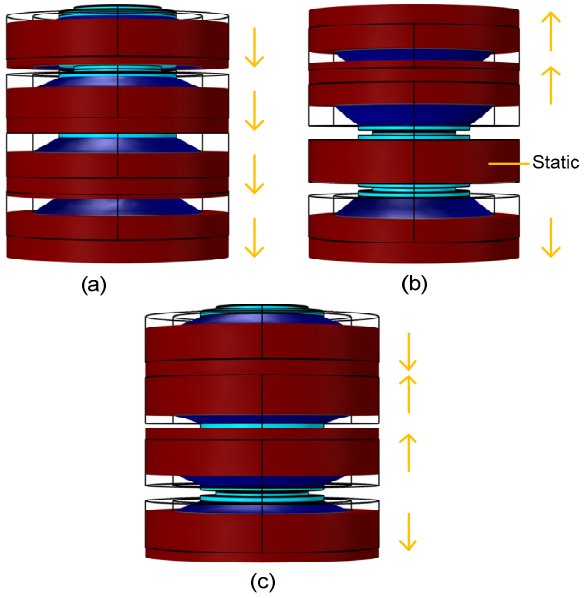


**Fig. 11 Modes of the three peaks**
(a) 42.1 Hz; (b) 47.2 Hz; (c) 47.6 Hz

The shielding zone without the rubber damping was 48–105 Hz, while that with the rubber damping was 44–105 Hz. The difference between these two results is small. However, the rubber damping will affect the amplitudes of the TSs. The calculation condition with damping in Fig. 10 includes damping of both the internal and external rubbers. To investigate the damping effect further, the effects of different damping on the transmission spectrum were studied (Fig. 12).

Fig. 12a shows the influence of the damping loss factor of the internal rubber when the loss factor of the external rubber is zero. The damping of the internal rubber has little influence on the characteristic frequencies. With the increase in the damping loss factor, the resonance of peak 1 becomes weakened while peaks 2 and 3 disappear. Moreover, the transmission spectrum increases slightly in the shielding zone. As the internal rubber almost stays still around the starting frequency of the first BG, the maximum attenuation in the shielding zone is nearly unchanged.

Fig. 12b shows the influence of the damping loss factor of the external rubber when the loss factor of the internal rubber is zero. The damping loss factor will weaken the resonance of peak 1 and make peaks 2 and 3 disappear. While the damping loss factor is less than 0.1, it has little effect on the characteristic frequencies. However, the shielding performance will disappear if the damping loss factor is over 0.5, as the vibration of the resonator is inhibited. The maximum attenuation decreases as the damping loss factor increases because the damping mitigates the vibration of the resonator.

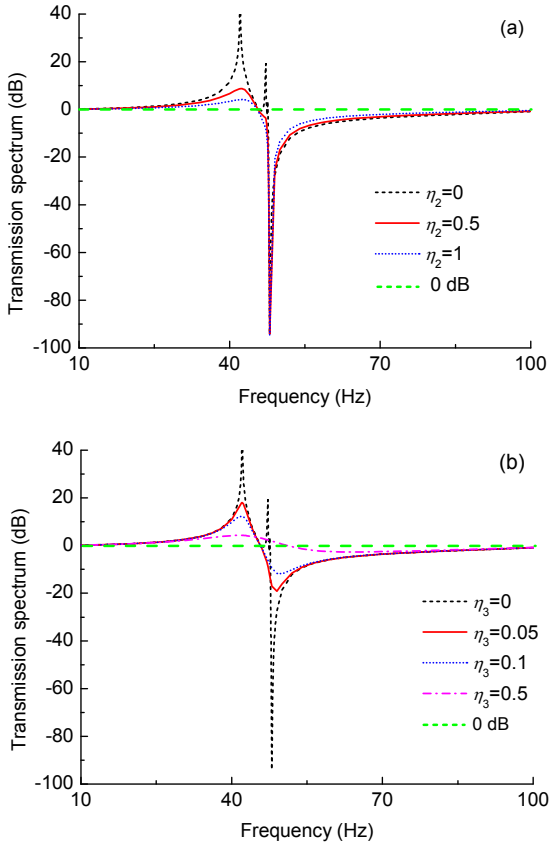


**Fig. 12 Effects of damping loss factors of internal rubber (a) and external rubber (b) on the transmission spectrum**

### 3.4 Vertical static stiffness of the metabarrier

As the bearing of the FST, the metabarrier should provide vertical stiffness for the floating slab. To retain the vibration isolation performance of a traditional FST, the vertical static stiffness of the metabarrier should be close to that of the existing bearings. He et al. (2015) tested the vertical static stiffness of a steel-spring vibration isolator, one of the most common bearings for floating-slabs in China. The stiffness was 5.3 kN/mm. The finite element software COMSOL Multiphysics was used to calculate the vertical static stiffness of the metabarrier. A vertical static load $F$ was applied to the upper end of the metabarrier while the lower end was constrained. The average displacement response $D$ of the upper end was measured and the vertical static stiffness obtained by the expression of $F/D$. The vertical static stiffness of the metabarrier was 6.0 kN/mm, which is close to that of existing steel-spring vibration isolators.

### 3.5 Overall vibration mitigation performance

The shielding performance of the BG and the vibration isolation performance of the low natural frequency can simultaneously contribute to the overall vibration mitigation performance of the new FST supported by the metabarrier. To investigate this overall vibration mitigation performance, we built a 3D half-track model of the new FST with the metabarrier (Fig. 13).

As the straight track and vertical wheel loads are symmetric about the same vertical plane, the half-track model and the symmetrical boundary condition were used to reduce the numbers of degrees of freedom. The symmetrical boundary condition was adopted at the symmetrical plane. Low-reflecting boundaries (LRB) were adopted at the ends of both the rail and the floating slab to decrease the effects of the reflected waves. All track components were modelled with solid elements, and the mesh size was sufficient for calculation below 120 Hz. A harmonic vertical force $F_{in}=F_0e^{i\omega t}$, where $F_0$ is the amplitude, was imposed on the mid-span rail head at the middle of the model, and the force $F_{out}$ transmitted to the infrastructure through the nearest metabarrier was measured. The force transfer rate (FTR) was used to reflect the overall vibration mitigation performance:

$$\mathrm{FTR}=20\lg\left(\frac{|F_{out}|}{F_0}\right). \tag{12}$$

With a lower FTR, the FST will have a better vibration mitigation performance. A 3D half-track model of a traditional FST was also built. The

steel-spring vibration isolator was modelled using a spring element with a vertical stiffness of 6.0 kN/mm. This was the same as the vertical static stiffness of the metabarrier. Parameters of the two models are listed in Table 2.

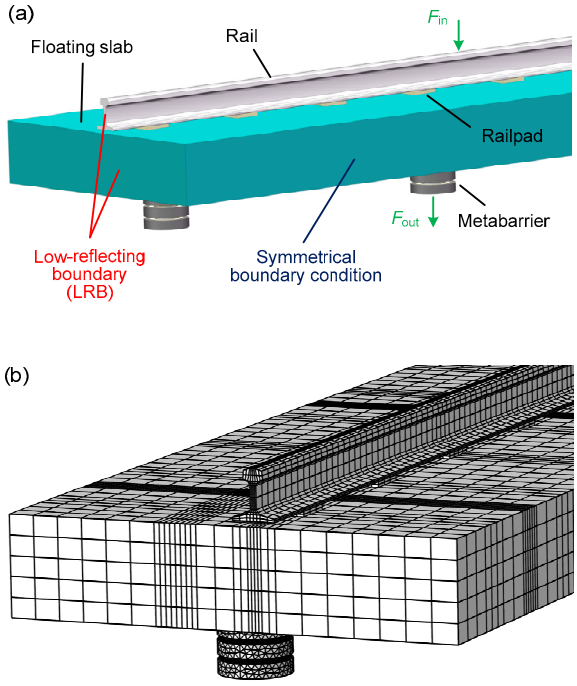


**Fig. 13 Half-track model of the new FST with metabarrier**
(a) Modelling; (b) Meshing

The results of the FTRs are shown in Fig. 14. The two FTR curves each had a peak at 24 Hz due to the bending resonance of the floating slab. Above 24 Hz, the FTR of the traditional FST decreased with the increase of the frequency. Thus, we focused mainly on the enhancement of the vibration mitigation performance at low frequencies at which the band gap produced by the metabarrier can take effect.

As the vertical static stiffness of the metabarrier is the same as that of the steel-spring vibration isolator, the FTRs of the two types of tracks below 40 Hz were close. Due to the shielding performance of the band gap, the FTR of the FST with the metabarrier was lower in the frequency range of 47–110 Hz, and therefore the vibration mitigation performance was enhanced. Furthermore, through the optimization of the band gap boundary frequencies, the frequency range of the enhancement could be controlled. In conclusion, the retained vibration isolation performance of the low natural frequency, the shielding performance of the band gap, and the controllability of band gap boundary frequencies all contributed to an improvement in overall vibration mitigation performance.

**Table 2 Parameters of the two half-track models**

| Track component | Parameter | Description |
|---|---|---|
| Rail | Rail section | CHN60 |
| | Elastic modulus (GPa) | 210 |
| | Mass density (kg/m$^3$) | 7850 |
| | Poisson's ratio | 0.3 |
| Railpad | Size (length×width ×height) (m) | 0.15×0.15×0.02 |
| | Spacing (m) | 0.625 |
| | Elastic modulus (MPa) | 44 |
| | Damping loss factor | 0.25 |
| | Mass density (kg/m$^3$) | 1300 |
| | Poisson's ratio | 0.47 |
| Floating slab | Full size (length× width×height) (m) | 5.00×3.20×0.35 |
| | Elastic modulus (GPa) | 35 |
| | Damping loss factor | 0.05 |
| | Mass density (kg/m$^3$) | 2500 |
| | Poisson's ratio | 0.2 |
| Metabarrier | Geometric and material parameters | Fig. 3 and Table 1 |
| | Spacing (longitudinal× lateral) (m) | 1.875×2.000 |
| Steel-spring vibration isolator | Vertical stiffness (kN/mm) | 6.0 |
| | Damping loss factor | 0.1 |

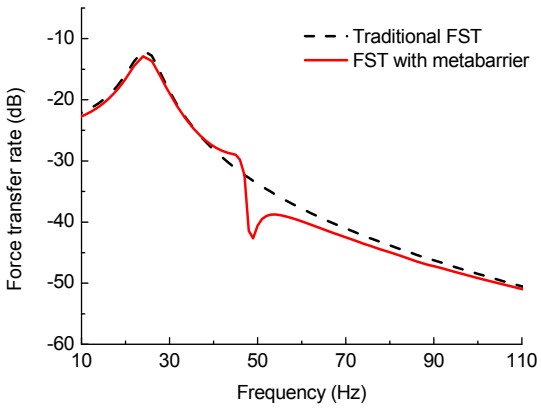


**Fig. 14 Force transfer rates of two types of tracks**

## 4 Optimization of band gap boundary frequencies

To generate a low-frequency BG, the LR phononic crystal mechanism was used in the metabarrier. A better shielding performance can be achieved if the dominant frequency range of ground-borne vibrations induced by subways is within a wider BG. As these vibrations are mainly in the low frequency range, a wider and lower BG is required for the optimization.

### 4.1 Single factor analysis on boundary frequencies

To obtain a wider and lower BG, single factor analysis was first conducted. The effects of a single factor on the first BG boundary frequencies were analysed using both the simplified models and the FEM (band structure). The results show that single factor changes of $a_4$ or $E_3$ cannot lead to both a wider and lower BG (Fig. 15). Single factor changes in other parameters will not cause conflicts in obtaining both a wider and lower BG.

Fig. 15 shows that the first BG boundary frequencies obtained by the simplified models and the FEM were similar. As the parameter $a_4$ varied from 20 mm to 36 mm, the starting frequency decreased, but the BG became narrower. As the parameter $E_3$ varied from 2 MPa to 3.6 MPa, the BG became wider, but the starting frequency increased. Hence, a multi-objective genetic algorithm was used to solve this multi-objective optimization problem (MOP).

### 4.2 Multi-objective optimization of the boundary frequencies

The objectives of the MOP were to lower the starting frequency and widen the BG:

$$\begin{cases} \min(f_{\mathrm{s}}), \\ \min\left(\dfrac{1}{f_{\mathrm{e}}-f_{\mathrm{s}}}\right), \end{cases} \tag{13}$$

where the expressions of $f_{\mathrm{s}}$ and $f_{\mathrm{e}}$ can be seen in Eq. (10). Parameters requiring optimization were $a_4$ and $E_3$, and the constraints of the parameters were as follows:

$$\begin{aligned} &25\ \mathrm{mm} \le a_4 \le 35\ \mathrm{mm}, \\ &1\ \mathrm{MPa} \le E_3 \le 4\ \mathrm{MPa}. \end{aligned} \tag{14}$$

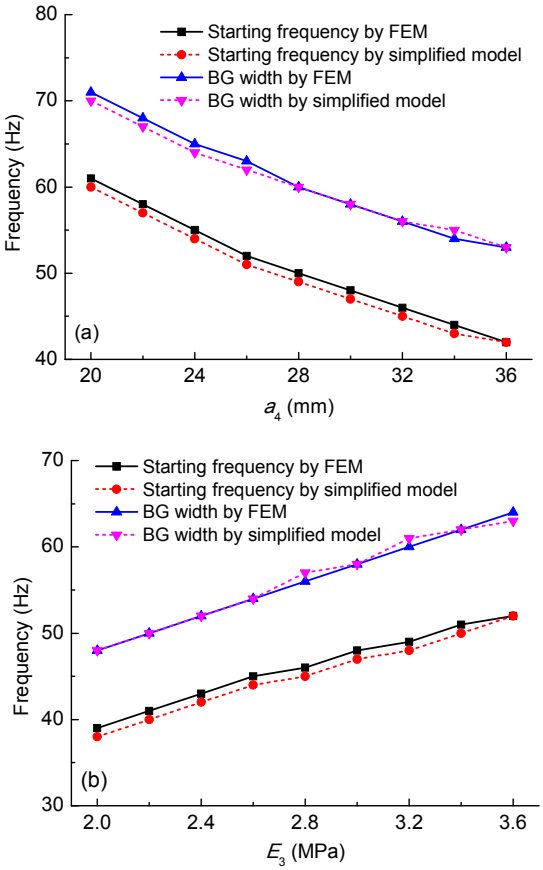


**Fig. 15 Effects of parameters $a_4$ (a) and $E_3$ (b) on the first BG boundary frequencies**

However, most MOPs do not lead to a single solution, but produce a set of solutions called a Pareto optimal set (Coello, 2006). If a solution to an MOP is Pareto optimal, there exists no other feasible solution which would decrease some criteria without causing a simultaneous increase in at least one other criterion. The vectors of the decision variables corresponding to the solutions included in the Pareto optimal set are called non-dominated. The Pareto front is the plot of the objective functions whose non-dominated vectors are in the Pareto optimal set. For practical applications, one or more solutions should be selected from the Pareto optimal set according to the understanding, knowledge, and preference of decision makers.

The non-dominated sorting genetic algorithm II (NSGA-II) was introduced by Deb et al. (2000). Due to its clever mechanisms, the NSGA-II has a good performance for MOPs. To solve the MOP of boundary frequencies, the Matlab optimization toolbox was adopted. The toolbox uses a controlled

elitist genetic algorithm which is a variant of NSGA-II. The Pareto Front of the MOP is shown in Fig. 16 and the partial Pareto optimums are listed in Table 3.

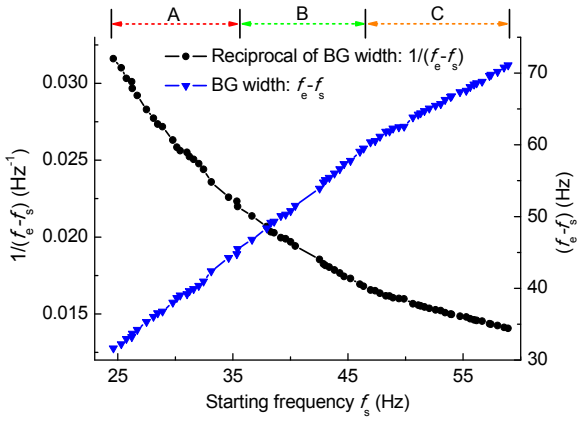


**Fig. 16 Pareto Front of the MOP**

**Table 3 Partial Pareto optimums of the MOP**

| $a_4$ (mm) | $E_3$ (MPa) | $f_s$ (Hz) | $f_e$–$f_s$ (Hz) |
|---|---|---|---|
| 33.4 | 3.76 | 49 | 62 |
| 31.0 | 3.56 | 50 | 63 |
| 31.8 | 3.79 | 51 | 64 |
| 30.9 | 3.79 | 52 | 65 |

If lowering of the starting frequency is the primary optimization objective, the solution can be selected from zone A of the Pareto front. If the widening of the BG is the primary optimization objective, the solution can be selected from zone C. If the two optimization objectives are of the same importance, the solution can be selected from zone B (Fig. 16).

However, the dominant frequency ranges of ground-borne vibrations induced by subways of different lines are not always the same. It is necessary to optimize the BG boundary frequencies according to the train-induced vibrations. Fig. 17 shows one third octave frequency spectrum of the measured train-induced vertical acceleration response on the tunnel wall in the subway line, with no vibration mitigation measures adopted in the measurement section.

The response was used as a survey to reflect the characteristics of ground-borne vibrations. There was a peak in the frequency range of 50–80 Hz (Fig. 17b), which was therefore the dominant frequency range. Thus, the starting frequency was chosen to be 50 Hz, and the corresponding optimal width of the BG was 63 Hz with the Pareto optimum of $a_4$=31.8 mm and $E_3$=3.79 MPa. As a result, the optimized BG frequency range (50–113 Hz) could cover this dominant frequency range of ground-borne vibrations and a better shielding performance was achieved. From the transmission spectrum analysis, the shielding zone using optimized parameters (without rubber damping) was 50–115 Hz, which matches well with the optimized BG frequency range.

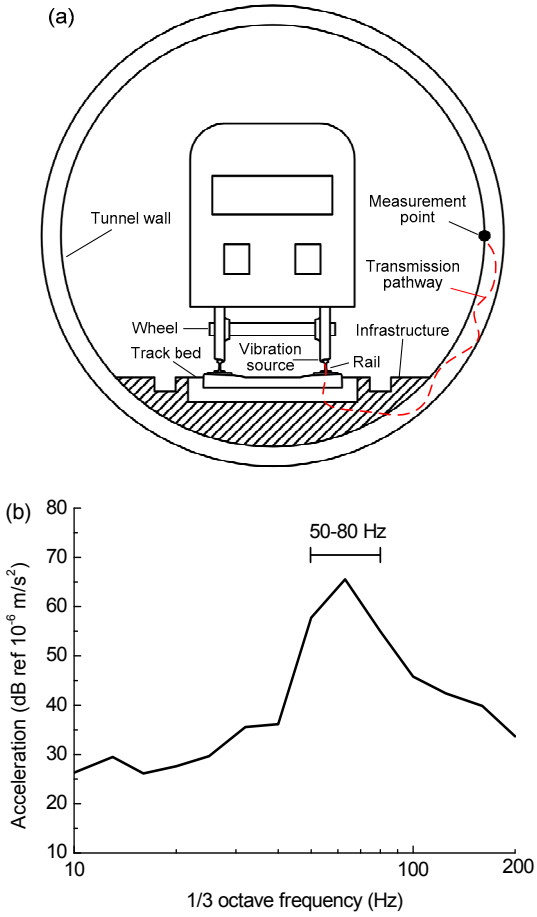


**Fig. 17 Train-induced vertical acceleration response on the tunnel wall**

(a) Layout of the measurement; (b) Result of the vertical acceleration response

## 5 Conclusions

In this paper, we propose a metabarrier based on a locally resonant mechanism for use as the bearing in a FST system. We also propose an optimization mechanism for the band gap boundary frequencies.

The following conclusions can be drawn from this work:

1. The metabarrier can generate a low-frequency locally resonant BG to shield infrastructure from the longitudinal waves from a floating slab. The vertical static stiffness of the metabarrier is close to that of existing steel-spring vibration isolators. The retained vibration isolation performance of the low natural frequency, the shielding performance of the band gap, and the controllability of band gap boundary frequencies all contribute to the overall vibration mitigation performance.

2. Simplified models showed that the starting frequency of the first BG is determined by the resonance of the steel resonator. In this resonance mode, the steel resonators of adjacent unit cells vibrate in inverse directions while the connectors and internal rubber almost stay still. The cut-off frequency of the first BG is determined by the resonance between the steel resonator and the combination of connectors and internal rubber. In this resonance mode, there is no relative motion between the connectors and the internal rubber. The steel resonator and the combination of the same unit cell vibrate in inverse directions.

3. The starting frequency will be affected by parameters which can change the shear stiffness of the external rubber or the mass of the steel resonator, while the cut-off frequency will be affected by parameters which can change the shear stiffness of the external rubber or the mass of the steel resonator, the connectors or the internal rubber. The vertical stiffness and the first BG boundary frequencies of the metabarrier can be independent.

4. The first BG frequency range matches well with the shielding zone obtained by the transmission spectrum. The damping of internal and external rubber has different effects on the transmission spectrum. An increase of the external rubber damping will decrease the maximum attenuation in the shielding zone, while an increase in the internal rubber damping has little effect on the maximum attenuation.

5. The simplified models can be used for the MOP to obtain a wider and lower BG. By the use of a genetic algorithm, the BG was chosen to be 50–113 Hz from the Pareto optimal set according to the dominant ground-borne vibrations induced by subways.

Future study will focus on an experimental verification of the band gap properties of the proposed metabarrier.

## References

Coello CCA, 2006. Evolutionary multi-objective optimization: a historical view of the field. *IEEE Computational Intelligence Magazine*, 1(1):28-36. https://doi.org/10.1109/MCI.2006.1597059

Deb K, Agrawal S, Pratap A, et al., 2000. A fast elitist non-dominated sorting genetic algorithm for multi-objective optimization: NSGA-II. International Conference on Parallel Problem Solving from Nature, p.849-858. https://doi.org/10.1007/3-540-45356-3_83

Ding DY, Gupta SS, Liu WN, et al., 2010. Prediction of vibrations induced by trains on line 8 of Beijing metro. *Journal of Zhejiang University-SCIENCE A (Applied Physics & Engineering)*, 11(4):280-293. https://doi.org/10.1631/jzus.A0900304

Ding DY, Liu WN, Li KF, et al., 2011. Low frequency vibration tests on a floating slab track in an underground laboratory. *Journal of Zhejiang University-SCIENCE A (Applied Physics & Engineering)*, 12(5):345-359. https://doi.org/10.1631/jzus.A1000276

Eringen AC, Suhubi ES, 1975. Elastodynamics, Volume II: Linear Theory. Academic Press, New York.

Gupta S, Degrande G, Lombaert G, 2009. Experimental validation of a numerical model for subway induced vibrations. *Journal of Sound and Vibration*, 321(3-5):786-812. https://doi.org/10.1016/j.jsv.2008.10.014

He QL, Wang JW, Chen ZG, et al., 2015. Stiffness and damping measurement of vibration isolator used for the metro floating slab. *Journal of Southwest University of Science and Technology*, 4:38-41 (in Chinese). https://doi.org/10.3969/j.issn.1671-8755.2015.04.009

Hui CK, Ng CF, 2009. The effects of floating slab bending resonances on the vibration isolation of rail viaduct. *Applied Acoustics*, 70(6):830-844. https://doi.org/10.1016/j.apacoust.2008.09.018

Kushwaha MS, Halevi P, Dobrzynski L, et al., 1993. Acoustic band structure of periodic elastic composites. *Physical Review Letters*, 71(13):2022-2025. https://doi.org/10.1103/PhysRevLett.71.2022

Kushwaha MS, Halevi P, Martínez G, et al., 1994. Theory of acoustic band structure of periodic elastic composites. *Physical Review B*, 49(4):2313-2322. https://doi.org/10.1103/PhysRevB.49.2313

Li ZG, Wu TX, 2008. Modelling and analysis of force transmission in floating-slab track for railways. *Proceedings of the Institution of Mechanical Engineers, Part F: Journal of Rail and Rapid Transit*, 222(1):45-57. https://doi.org/10.1243/09544097JRRT145

Liu CC, Jing XJ, Chen ZB, 2016. Band stop vibration suppression using a passive X-shape structured lever-type isolation system. *Mechanical Systems and Signal Processing*, 68-69:342-353. https://doi.org/10.1016/j.ymssp.2015.07.018

Liu M, Li P, Zhong YT, et al., 2015. Research on the band gap characteristics of two-dimensional phononic crystals

microcavity with local resonant structure. *Shock and Vibration*, 2015:239832.
https://doi.org/10.1155/2015/239832

Liu ZY, Zhang XX, Mao YW, et al., 2003. Locally resonant sonic materials. *Science*, 289(5485):1734-1736.
https://doi.org/10.1126/science.289.5485.1734

Mead DM, 1996. Wave propagation in continuous periodic structures: research contributions from Southampton, 1964-1995. *Journal of Sound and Vibration*, 190(3): 495-524.
https://doi.org/10.1006/jsvi.1996.0076

Sanayei M, Maurya P, Moore JA, 2013. Measurement of building foundation and ground-borne vibrations due to surface trains and subways. *Engineering Structures*, 53: 102-111.
https://doi.org/10.1016/j.engstruct.2013.03.038

Wang P, Yi Q, Zhao CY, et al., 2017. Wave propagation in periodic track structures: band-gap behaviours and formation mechanisms. *Archive of Applied Mechanics*, 87(3):503-519.
https://doi.org/10.1007/s00419-016-1207-8

Xiao XB, Li YG, Zhong TS, et al., 2017. Theoretical investigation into the effect of rail vibration dampers on the dynamical behaviour of a high-speed railway track. *Journal of Zhejiang University-SCIENCE A (Applied Physics & Engineering)*, 18(8):631-647.
https://doi.org/10.1631/jzus.A1600697

Yan Y, Cheng Z, Menq F, et al., 2015. Three dimensional periodic foundations for base seismic isolation. *Smart Materials and Structures*, 24(7):075006.
https://doi.org/10.1088/0964-1726/24/7/075006

Yao ZJ, Yu GL, Wang YS, et al., 2010. Propagation of flexural waves in phononic crystal thin plates with linear defects. *Journal of Zhejiang University-SCIENCE A (Applied Physics & Engineering)*, 11(10):827-834.
https://doi.org/10.1631/jzus.A1000123

Yin J, Huang J, Zhang S, et al., 2014. Ultrawide low frequency band gap of phononic crystal in nacreous composite material. *Physics Letters A*, 378(32-33):2436-2442.
https://doi.org/10.1016/j.physleta.2014.06.021

Zhao HJ, Guo HW, Gao MX, et al., 2016. Vibration band gaps in double-vibrator pillared phononic crystal plate. *Journal of Applied Physics*, 119(1):014903.
https://doi.org/10.1063/1.4939484

Zheng L, Li YN, Baz A, 2011. Attenuation of wave propagation in a novel periodic structure. *Journal of Central South University of Technology*, 18(2):438-443.
https://doi.org/10.1007/s11771-011-0715-5

## 中文概要

**题　目：超屏障在工程结构纵波抑制中的应用：带隙特性及优化机理**

**目　的：**提出一种基于局域共振带隙机理的超屏障，并将其应用于地铁浮置板轨道结构中。在保留现有浮置板轨道隔振效果的同时，进一步抑制低频带隙频率范围内纵波从道床板往基底的传播。

**创新点：**1. 探究超屏障导波模态，获取其带隙频率范围，建立带隙边界频率的简化模型；2. 建立三维半轨道模型，分析新型浮置板轨道结构的整体减振效果；3. 提出一种基于现场测试结果的超屏障带隙频率范围优化机理。

**方　法：**1. 采用有限元法，筛选沿轴向传播的纵波模态，推导带隙边界频率计算公式；2. 通过计算传递谱，研究超屏障结构的纵波抑制效果；3. 建立三维半轨道模型，计算力传递率，并研究采用超屏障的浮置板轨道结构的整体减振效果；4. 基于带隙边界频率计算公式，采用多目标遗传算法，得到超屏障关键参数的 Pareto 最优解集，并依据现场测试结果选取关键参数最优解。

**结　论：**1. 所保留的现有浮置板轨道隔振效果、超屏障的纵波抑制效果以及带隙频率范围的可控性均有助于提高新型浮置板轨道的整体减振效果。2. 超屏障可提供与现有浮置板轨道隔振器相近的静垂向刚度，且该静垂向刚度与第一带隙频率范围是相互独立的。3. 简化模型及边界频率计算公式可用于获取具有更低起始频率且更宽频率范围的带隙；结合多目标遗传算法及现场测试结果，选取了第一带隙为 50~113 Hz 的最优解。

**关键词：**超屏障；声子晶体；带隙；纵波；优化机理